This is a preprint, the final version is subject to change, of the American Mineralogist (MSA)
Cite as Authors (Year) Title. American Mineralogist, in press.
(DOI will not work until issue is live.) DOI: http://dx.doi.org/10.2138/am.2014.4674

Visible and Short Wave Infrared Reflectance Spectroscopy of REE Fluorocarbonates

DAVID J. TURNER[1,*], BENOIT RIVARD[2], LEE A. GROAT[1]

[1]Department of Earth, Ocean and Atmospheric Sciences, University of British Columbia, Vancouver, British Columbia V6T 1Z4, Canada

[2] Department of Earth and Atmospheric Sciences, University of Alberta, Edmonton, Alberta T6G 2E3. Canada

*E-mail: dturner@eos.ubc.ca

ABSTRACT

The mineralogy of rare earth element deposits is critical in understanding their petrogenesis and has significant implications for their economic viability. Lanthanide-bearing compounds are known to produce sharp absorption features in the visible to short wave infrared region (VIS-SWIR), however, a significant knowledge gap exists between the fields of hyperspectral reflectance spectroscopy and rare earth element mineralogy. Reflectance spectra were collected from four bastnaesite samples, two parisite samples and one synchysite sample from the visible into the shortwave infrared. These REE fluorocarbonate mineral samples were characterized via scanning electron microscopy and electron probe microanalysis. Sharp absorptions of REE-bearing minerals are mostly the result of 4*f*-4*f* intraconfigurational electron transitions and for the light REE-enriched fluorocarbonates, the bulk of the features can be ascribed to Nd^{3+}, Pr^{3+}, Sm^{3+} and Eu^{3+}. The lanthanide-related spectral responses of the REE fluorocarbonates are consistent across the group, supporting the notion that the REE cation site is

very similar in each of these minerals. Carbonate-related spectral responses differed between these minerals, supporting the notion that the crystallographic sites for the carbonate radical differ between bastnaesite, synchysite and parisite. Exploitable spectral differences include a distinct absorption band at 2243 nm that separates bastnaesite from synchysite and parisite. Similarly, for bastnaesite a dominantly Pr^{3+} related absorption band located is at 1968 nm while in synchysite and parisite it occurs at 1961 nm.

Keywords: Mineral spectroscopy, rare earth elements, hyperspectral, bastnaesite, parisite, synchysite

INTRODUCTION

The mineralogy of rare earth element deposits is critical in understanding their petrogenesis and has significant implications for their economic viability. Rapid determination of ore modal mineralogy for these deposit types by hyperspectral reflectance spectroscopy would provide immediate feedback on the strength, type and relevance of mineralization. Lanthanide-bearing compounds are known to produce sharp absorption features in the visible to short wave infrared region (VIS-SWIR) and have been conventionally viewed as unchanging features in the field of remote sensing (e.g., Clark 1999); however, a significant knowledge gap exists between the fields of hyperspectral reflectance spectroscopy and rare earth element mineralogy.

The lanthanides (*Ln*) are a series of 15 elements belonging to the *4f* block of the periodic table, and from lightest to heaviest are lanthanum (La), cerium (Ce), praseodymium (Pr), neodymium (Nd), promethium (Pm), samarium (Sm), europium (Eu), gadolinium (Gd), terbium (Tb), dysprosium (Dy), holmium (Ho), erbium (Er), thulium (Tm), ytterbium (Yb) and lutetium (Lu). In geological environments the lanthanides are commonly found together in their trivalent state, with the exception of divalent europium

48 (Eu^{2+}) and sometimes tetravalent cerium (Ce^{4+}). The term "rare earth elements" (REE) comprises the
49 lanthanides, commonly yttrium (Y) and sometimes scandium (Sc) due to similar chemical
50 characteristics. Coordination states of the REE cations in the assorted mineral structures can be quite
51 variable (e.g., Miyawaki and Nakai 1996), ranging from a reasonably symmetrical 8-coordinated site in
52 xenotime, to britholite with two distinct sites with coordination numbers of 7 and 9, and the REE
53 fluorocarbonates with multiple bonding anions (oxygen and fluorine) with a coordination number of 9
54 (6O+3F).
55
56 The mineralogy of REE ore deposits is important because the metallurgy of only certain REE-bearing
57 phases is well established. Namely, most global REE production is derived from REE fluorocarbonate
58 minerals (e.g., bastnaesite, parisite and synchysite), REE phosphate minerals (e.g., monazite and
59 xenotime) and from ion-absorbed clays, however, recent advances have been made in the treatment of
60 REE silicate mineral ore (e.g., eudialyte and britholite) (e.g., Mariano and Mariano 2012). Furthermore,
61 REE deposits can show a complex mineral paragenesis with REE-mineral assemblages varying
62 significantly across a single geological system. Consequently, there exists significant potential for
63 reflectance spectroscopy to play an important role in the exploration and exploitation of REE ore
64 deposits.
65
66 The objectives of this study are to present mineralogical characterization and reflectance spectra in the
67 visible to short wave infrared region of the main rare earth element fluorocarbonate minerals;
68 bastnaesite, parisite and synchysite. Following mineralogical and spectroscopic background of REE
69 bearing minerals we provide a band registry for these minerals as well as interpretations of spectral
70 absorption features related to the lanthanides. The spectral features of the registry will be the focus of

71 further study in the development of hyperspectral reflectance imaging spectroscopy to carry out REE
72 mineral identification, REE mineral abundance estimates and rare earth element abundance estimates.
73

74 **GENERAL SPECTROSCOPY OF THE LANTHANIDES**

75 The outer radius of the 4*f* electron shells (~0.3 Å) for the lanthanides is much less than that of their filled
76 5*s* and 5*p* shells (~2 Å, ~1 Å). It can then be approximated that the local electronic environment of Ln^{3+}
77 cations interacts primarily with those outer shells, leaving the 4*f* electrons 'relatively sheltered' but not
78 completely non-participatory in bonding (e.g., Liu, 2005). Electrostatic repulsion of the base ion
79 generates a first level splitting of spectroscopic states, $^{2S+1}$L (e.g., ^{5}I). Next, spin-orbit coupling splits
80 these into multiplets, or "J-levels" (e.g., $^{5}I_{8}$), and once placed into a crystal field the J-levels are then
81 split into "Stark Sublevels". Crystal field interactions for the *Ln* cation include variables such as ligand
82 type, coordination number and polyhedron asymmetry which all play a role in the location and intensity
83 of energy levels and the associated absorption (Görller-Walrand and Binnemans, 1998). Each of the
84 resulting sublevels provides the potential for promotion of a relaxed electron into an excited state, giving
85 rise to absorption of electromagnetic radiation (e.g., light) at a specific energy level (e.g., wavelength).
86

87 The spectroscopy of REE-bearing phases is well established in the fields of physics and chemistry,
88 however, the well understood principles and well studied doped compounds do not lend to direct
89 translation into mineralogy and hyperspectral remote sensing. For example, the Dieke Diagram (Dieke
90 *et al.* 1968) details intraconfigurational *4f-4f* transitions for 'free ions' as deduced through studies of
91 largely mono-lanthanide synthetic compounds, however, the transitions shown do not include splitting of
92 energy levels due to a crystal field nor the complexities of naturally occurring REE minerals with
93 variable REE distributions and other elemental substitutions. Consequently, this diagram and other band

94 registries can only act as proxies to help identify origins of absorption features in reflectance spectra
95 from minerals.
96
97 In general, and excluding other physical parameters such as grain size, the strength of absorption
98 features by the lanthanides will be primarily a function of the concentration of the ion as well as the
99 specific absorptivity of that ion's intraconfigurational transitions within a given crystal structure. The
100 location of lanthanide-related absorption features will be primarily a function of the cation's specific
101 coordination and asymmetry in the host crystal structure.

102 REVIEW OF REE-RELATED REFLECTANCE SPECTROSCOPY STUDIES

103 Few studies have been published addressing rare earth element bearing minerals and rocks in the field of
104 reflectance spectroscopy. Surveys of carbonatites and alkaline intrusive complexes in the literature can
105 be divided into coarse spectral resolution spaceborne studies (e.g., Oppenheimer 1998, Rowan and Mars
106 2003, Mars and Rowan 2011), fine spectral resolution airborne studies (e.g., Crowley *et al.* 1988, Rowan
107 *et al.* 1995, Bowers and Rowan 1996, Bedini 2009), and fine resolution ground and lab-based studies
108 (e.g., Rowan *et al.* 1986, McHugh *et al.* 2000). The early work by Rowan, Crowley and Mars recognized
109 the potential of exploiting REE absorption features with hyperspectral imaging, however, focus of their
110 future research shifted to other geological systems, use of ASTER multispectral satellite imagery, and
111 planetary remote sensing.
112
113 The studies with coarse resolution used ASTER imagery and were focused on lithological mapping via
114 endmember extraction and band ratios. The general results are that lithologies of carbonatite complexes
115 can be identified with moderate confidence using ASTER satellite data from areas with well-established
116 geological maps (e.g., Khanneshin, Mountain Pass, Ol Doynio Lengai). Remote sensing using the finer

resolution AVIRIS airborne system shows improved classification of rock types and even interpreted detection of REE from Mountain Pass (e.g., Crowley *et al*., 1988). Bedini (2009) investigated the REE-mineralized Sarfatoq carbonatite complex of Greenland using the HyMap airborne hyperspectral imager focusing on the classification of rock type and predictive mapping, however, there was no mention of any specific REE phases being detected from the airborne platform. Similar results were achieved by Bowers and Rowan (1996) at the Ice River Complex using AVIRIS data. Ground and laboratory based studies by Rowan *et al.* (1986) of four carbonatite hosted rare metal deposits focused on rock type classification and were able to discriminate between several carbonatite phases, as well as identify the sharp absorption features caused by Nd^{3+} in field samples. This earliest work is referenced in all of the above literature and has served as a base for the spectral classification of rock types at carbonatite and alkaline intrusive igneous complexes.

Early infrared spectroscopy investigations of carbonate minerals by Adler and Kerr (1963) included bastnaesite and parisite because of their distinct carbonate arrangements, but did not investigate the influence of the lanthanides and stopped short of the shortwave infrared region. The benchmark mineral spectroscopy paper of Hunt (1977) lists monazite (misspelled as monzonite) in his tabulation of common minerals and respective spectral signatures, however, La^{2+} is listed as the origin of absorptions but La would have 3+ valence in monazite and would therefore not have spectral features in the VIS-SWIR (e.g., Liu 2005). Clark (1999) covers several REE oxides in his Spectroscopy of Rocks and Minerals review and recognizes that the patterns seen in REE minerals are a combination of several lanthanides but states that absorptions are independent of mineralogy. Reflectance spectra in the VNIR-SWIR of bastnaesite and parisite with limited discussions have been presented by Kerr *et al.* (2011) and Morin-Ka

(2012), with both publications stating that REE signatures are present in these REE minerals and that more detailed documentation is warranted.

CRYSTAL STRUCTURE REVIEWS OF BASTNAESITE, PARISITE AND SYNCHYSITE

Bastnaesite, parisite and synchysite are rare earth element fluorocarbonate minerals of economic significance in many REE deposits and occurrences. Bastnaesite, $CeCO_3F$, is the most commonly reported of these minerals, however, it is also the most familiar of the group. Synchysite, $CaCe(CO_3)_2F$, is the most Ca-enriched of the REE fluorocarbonates, sometimes forms euhedral prismatic crystals and is the second most reported. Parisite, $CaCe_2(CO_3)_3F_2$, can form distinct doubly terminated pyramidal crystals and is the least reported of these rare earth fluorocarbonate minerals. Rontgenite, $Ca_2Ce_3(CO_3)_5F_3$, is another rare REE fluorocarbonate mineral with a similar structure but was not addressed in this study.

Total rare earth oxide (REE_2O_3) content increases from ~52 wt% in Ca-rich synchysite, to ~60 wt% in parisite and up to ~75 wt% in Ca-absent bastnaesite. These minerals show preference for the light rare earth elements (LREE) and have similar slopes and trends in Chondrite-normalized diagrams. These three minerals are commonly found together, are structurally related, can show syntaxial intergrowth and are also commonly found together in secondary mineral mixtures.

Structurally, each of the phases can be assembled using a common set of building blocks (Ni *et al.* 1993), which include layers of CeF, CO_3, and Ca. On an atom basis, bastnaesite is Ca-absent, parisite shows REE:Ca=2:1 and synchysite shows REE:Ca=1:1. Accordingly, the stacking order of the blocks gives rise to the different compositional proportions and mineral species (Fig. 1). Polytypism has been

documented for these minerals (e.g., Meng *et al.* 2001). It is important to note that all of the REE will occur in the Ce site but only Ce will be listed for brevity. Table 1 documents some basic crystallographic data for the REE fluorocarbonates.

In bastnaesite Ni *et al.* (1993) described the hexagonal crystal structure as being built by layers of REE-F alternating with layers of CO_3 in (0001) arrangement. There is one REE site, which is coordinated with 3 in-plane fluorine (F) atoms and two sets of 3 oxygen (O) atoms from bordering CO_3 layers. Bond lengths of REE with O are reported at 2.591, 2.542 and 2.579 Å while lengths with F are shorter and between 2.403 and 2.416 Å. The resulting 9-coordinated tricapped trigonal prismatic REE site is therefore asymmetrical with two distinct sets of bonding ligands and lengths.

Ni *et al.* (2000) studied the crystal structure of parisite and determined that, unlike bastnaesite, it is monoclinic. The structure was described as being built of two portions of bastnaesite layers connected by a Ca layer, stacked along the c-axis (i.e., CeF-CO_3, CeF-CO_3, Ca-CO_3). Coordination for REE is similar to bastnaesite (3 x Ce-F, 6 x Ce-O) with Ce-O mean lengths between 2.55 and 2.57 Å and Ce-F means between 2.38 and 2.41 Å. Minimum and maximum Ce-O bond lengths are 2.47 and 2.63 Å, while for Ce-F they are 2.37 and 2.45 Å. The resulting 9-coordinated tricapped trigonal prismatic REE site is therefore asymmetrical with two distinct sets of bonding ligands and lengths. The unit cell for parisite contains three carbonate radical layers, two of which are influenced by both the REE-F and Ca layers and one of which is influenced only by REE-F layers.

The crystal structure of synchysite, $CaCe(CO_3)_2F$, was investigated by Liben *et al.* (1994) and expanded upon by Ni *et al.* (2000). Synchysite is also monoclinic and is built by stacking layers of CeF-CO_3 and

185 Ca-CO_3 in a one-to-one ratio along (001), making it the most Ca-rich member of the REE
186 fluorocarbonate group. Coordination for REE is similar to bastnaesite and parisite (3 x Ce-F, 6 x Ce-O)
187 with Ce-O mean lengths between 2.557 and 2.567 Å and Ce-F means between 2.394 and 2.407 Å.
188 Minimum and maximum Ce-O bond lengths are 2.50 and 2.62 Å, while for Ce-F they are 2.38 and 2.41
189 Å. The resulting 9-coordinated tricapped trigonal prismatic REE site is therefore asymmetrical with two
190 distinct sets of bonding ligands and lengths. In the case of synchysite, the carbonate layer is now always
191 influenced by bonding with both Ca and REE-F layers.
192
193 Each of the REE fluorocarbonate minerals hosts REE in 9 fold tricapped trigonal prismatic coordination
194 with 6 oxygen atoms at the apices of the prism and 3 fluorine atoms in planar configuration through the
195 faces of the prism (Fig. 1). Minor differences in the bond lengths of REE-F and REE-O amongst the
196 REE fluorocarbonates are reported in the literature, however, a significant difference between each of
197 the minerals is the local environment surrounding the carbonate radical. In bastnaesite, the oxygen
198 apices of the CO_3 radical interact only with REE cations both below and above the CO_3 plane. In
199 parasite, two of the three repeating CO_3 layers interact with REE and Ca above and below the plane
200 while the third repeating CO_3 layer interacts only with REE. For synchysite, the apices of the CO_3
201 radical always interact with both REE and Ca on either side of the plane. Consequently, bastnaesite and
202 synchysite show only one configuration for cation bonding with the CO_3 radical whereas parasite shows
203 two configurations that are unevenly populated. Furthermore, the geometry of the CO_3 polyhedra is
204 much more variable for parisite than for synchysite or bastnaesite (Fig. 2, Table 1).
205
206 The cation sites for REE in these minerals are very similar and one would therefore expect that the
207 spectral features due to intraconfigurational electron transitions of the REE would also be very similar. It

would then be expected that ***variations between spectra of the same mineral*** would be predominantly in the relative strengths of REE-specific absorption features while ***variations of REE-related spectral features between the different minerals*** might include slight shifts in the locations of REE-related absorption features as well as the strength of some of these features. The coordination environment of the carbonate radical is quite different for each of these minerals, relatively speaking, and one would expect to see a difference in the carbonate related absorption features between the minerals. Other variables that may influence spectra include the signal to noise ratio of the spectral data, crystallographic orientation, variations in other trace elements, and possibly syntaxial intergrowths with other REE fluorocarbonates.

The infrared spectra of bastnaesite and parisite were presented in Adler and Kerr (1963). Bastnaesite is characterized by carbonate related absorptions common to what is seen in calcite and dolomite, however, the strongest features for bastnaesite are the $\nu_2(CO_3)$ and $\nu_3(CO_3)$ modes at 11.52 μm (868 cm^{-1}) and 6.93 μm (1443 cm^{-1}), respectively, and are asymmetric. The $\nu_2(CO_3)$ and $\nu_3(CO_3)$ modes in parisite are the most prominent and are located at 11.49 μm (870 cm^{-1}) and 6.90 μm (1449 cm^{-1}), respectively, and are asymmetric. Both the $\nu_2(CO_3)$ and $\nu_3(CO_3)$ absorption features are broader for parisite than for bastnaesite. For parisite Adler and Kerr (1963) also made note of the multiple non-equivalent carbonate radicals and observed doublets for the $\nu_1(CO_3)$ (9.19 and 9.27 μm, or 1088 and 1079 cm^{-1}) and $\nu_4(CO_3)$ (13.40 and 13.62 μm, or 746 and 734 cm^{-1}) vibrational modes while the $\nu_1(CO_3)$ and $\nu_4(CO_3)$ modes for bastnaesite occur at 9.21 μm and 13.74 μm (1086 and 728 cm^{-1}). Raman and infrared spectroscopy studies by Frost and Dickfos (2007) and Yang *et al.* (2008) revealed that OH stretching bands are present in most REE-fluorocarbonate samples studied, although the bands recorded are variable in number and position.

231 **EXPERIMENTAL METHODS**

232 **Samples**

233 Three bastnaesite samples were borrowed from the Canadian Museum of Nature's Mineral Collection
234 (CMNMC) and were labeled as originating from Burundi (#39382), the Karonga Mine (Congo, #56255)
235 and Madagascar (#50588). These samples were all single crystal fragments, honey brown in colour, and
236 approximately 1 cm^3. A fourth bastnaesite crystal sample from the Diao Lou Shan area in Sichuan
237 (China) was obtained from A. Mariano, was light brown in colour and measured 3 x 3 x 2 cm. Two
238 sample sets of parisite crystals from Snowbird (Montana, USA) and Muzo (Colombia) were obtained
239 from A. Mariano. The Snowbird set comprised four euhedral elongate tapering prismatic crystal
240 fragments, each approximately 1 x 1 x 2.5 cm and light grey-brown in colour. The Muzo set comprised
241 two euhedral tapering prismatic crystal fragments, each approximately 0.5 x 0.5 x 0.5 cm and golden
242 brown with high translucency. Scanning electron microscopy (SEM) investigations showed that all the
243 bastnaesite and parisite samples were not compositionally zoned, did not show syntaxy, and did not
244 show any other mineral inclusions. Three samples of synchysite were studied, originating from
245 Narsarsuk (South-west Greenland, #UBC-3376), the White Cloud Mine (Colorado, USA) and Morris
246 County (New Jersey, USA). Both the White Cloud Mine (from CMNMC, #37320) and Morris County
247 (from CMNMC, #37321) samples were fine grained and SEM investigations showed that the complex
248 mineralogy was not suitable for baseline spectroscopic characterization studies. The Narsarsuk hand
249 sample (from UBC Museum Collection) included a cluster of ~25 light brown elongate prismatic
250 euhedral synchysite grains up to ~1 mm long, hosted on a feldspar-biotite dominated matrix. SEM
251 examination and electron microprobe analyses (EMPA) data also revealed very minor amounts of
252 ancylite and an unknown REE-Ca-Sr-Ba phase. Reagent-grade lanthanide oxide powders and REE-

253 doped spectralon wavelength calibration samples were also investigated in order to aid in band
254 assignment.

255 **Reflectance spectroscopy**

256 Reflectance spectroscopy was primarily carried out using the sisuROCK instrumentation (manufactured
257 by SPECIM Spectral Imaging Ltd.) at the University of Alberta's CoreSensing Facility, and data was
258 handled using ENVI 4.4, a widely used and commercially available software package. Two imaging
259 spectrometers ("cameras") acquired reflectance spectra in the visible-near infrared (VNIR, 396 nm to
260 1003 nm over 784 channels for an average spectral resolution of 0.77 nm) and shortwave infrared
261 (SWIR, 928 nm to 2530 nm over 256 channels for an average spectral resolution of 6.26 nm) portions of
262 the electromagnetic spectrum in high spatial resolution mode. Spatial resolution of the cameras in this
263 mode was approximately 0.079 mm / pixel in the VNIR and 0.241 mm / pixel in the SWIR. Noise was
264 very prevalent in the shortest wavelength portion of the VNIR camera below ~550 nm and moderate
265 from 550 nm to ~650 nm. In the high spatial resolution mode, averaging ~16 pixels resulted in reliable
266 spectra in the noisier ranges that would be useable in spectral libraries. Spectra presented originate from
267 single crystals for parisite and bastnaesite. The synchysite spectrum is an aggregate of multiple single
268 crystals. The euhedral crystals of bastnaesite from Sichuan, parisite from Muzo, and parisite from
269 Snowbird were also large enough to permit imaging both parallel and perpendicular to the grains' *c*-axis.
270 Spectra documented here are nominally an average of 2004 pixels for the VNIR camera and 1029 pixels
271 for the SWIR camera. Samples were placed on a matte black surface that translates the samples under
272 the camera and has very low reflectance across the sampled wavelength range. Some samples were
273 propped up with foam blocks to ensure surfaces of interest faced the spectrometers. All samples were
274 also substantially thick enough to assume the reflectance spectra are representative of the mineral target.
275

A TerraSpec Pro point spectrometer manufactured by Analytical Spectral Devices Inc. (ASD) was used in the earliest studies and records 2151 channels from 350 to 2500 nm, for a spectral resolution of ~1 nm. Spot size of the point spectrometer is approximately 1 cm in diameter, which significantly restricted the use of this instrument. Methodology of acquiring spectra followed the manufacturer's recommendation of ~30 second acquisition time with periodic darkfield and white reference spectralon panel normalization and wavelength calibrations using Ho, Er and Dy doped spectralon samples (manufactured by Labsphere). Though the ASD instrument provided limited spectra (e.g., for bastnaesite from Mountain Pass), they were valuable for confidence in band assignment below 600 nm because of lower noise levels than using the sisuROCK system.

Averaged spectra from the imaging spectrometer were preferred over spectra from the spot spectrometer because some of the samples investigated had grain sizes smaller than were confidently resolvable by the point spectrometer. This allowed for non-destructive testing of mineral specimens and the ability to exclude spectral effects from other minerals that would have otherwise been in the field of view of the spot spectrometer. For larger single crystal samples, a simple Region Of Interest (ROI) was used to select the target mineral's pixels for averaging. For finer grained samples, a priori knowledge about the sample allowed several baseline spectra to be isolated from single pixels. These spectra were then used to run mixture tuned matched filtering within the ENVI software package on the entire scene, from which a strict qualitative threshold allowed a discrete selection of pixels to be averaged (see Fig. 3). Reflectance spectra did not have the continuum removed so as to present the data unmodified and to facilitate comparison against other earlier publications.

297 **Scanning electron microscopy and electron microprobe analysis**

298 The Philips XL30 scanning electron microscope (SEM) at the University of British Columbia, which is
299 equipped with an energy-dispersion X-ray spectrometer (EDS), was used for preliminary examination of
300 mineral mounts of selected minerals and rock fragments studied by reflectance spectroscopy.
301
302 Selected samples were then analyzed by electron microprobe at the Saskatchewan Research Council's
303 Advanced Microanalysis Centre using a Cameca SX-100 equipped with 5 tunable wavelength dispersive
304 spectrometers. Operating conditions were: 40° takeoff angle, beam energy of 15 keV, beam current of 20
305 nA, beam diameter of 5 μm. The MAN background intensity data was calibrated and continuum
306 absorption corrected. Elements were acquired using analyzing crystals **LLIF** for Fe*K*α, Ta*L*α, Pr*L*α,
307 Eu*L*α, Dy*L*α, Tm*L*α, Mn*K*α, La*L*α, Nd*L*α, Gd*L*α, Ho*L*α, Yb*L*α, Ba*L*α, Ce*L*α, Sm*L*α, Tb*L*α, Er*L*α, Lu*L*α,
308 **PET** for Ca*K*α, K*K*α, Cl*K*α, Ti*K*α, Nb*L*α, Y*L*α, Sr*L*α, Zr*L*α, P*K*α, U*M*α, Th*M*α, and **LTAP** for Mg*K*α,
309 F*K*α, Na*K*α, Si*K*α, Al*K*α. Counting times were 10 seconds for Zr and P and 15 seconds for all other
310 elements, with off peak count times of 10 seconds. The standards (with elements) were SPI-Barite (Ba),
311 SPI-Celestite (Sr), SPI-YAG (Y, Al), Smithsonian Cr-augite (Mg, Ca), Smithsonian Ilmenite (Fe, Ti),
312 Smithsonian Apatite (F, P), Smithsonian Microcline (K), Smithsonian Zircon (Zr), Harvard Albite (Si,
313 Na), Cameca Mn (Mn), SPI2-TlCl (Cl), SPI2-Nb (Nb), SPI2-La (La), SPI2-Ce (Ce), SPI2-Pr (Pr), SPI2-
314 Nd (Nd), SPI2-Sm (Sm), SPI2-Eu (Eu), SPI2-Gd (Gd), SPI2-Tb (Tb), SPI2-Dy (Dy), SPI2-Ho (Ho),
315 SPI2-Er (Er), SPI2-Tm (Tm), SPI2-Yb (Yb), SPI2-Lu (Lu), SPI2-Ta (Ta), SPI2-Th (Th), and SPI2-U
316 (U). Amounts of CO_2 (as CO_3) and OH^- (as H_2O) were determined by stoichiometry based on 4, 11 and
317 7 anions for bastnaesite, parisite and synchysite, and for full occupation of the F atomic site by F^-, Cl^-
318 and OH^-.

RESULTS

Samples described here were selected from a larger set and were characterized by imaging reflectance spectroscopy, scanning electron microscopy and microprobe analysis. Several samples have spectra collected from a point spectrometer. Table 2 documents electron microprobe results for the REE fluorocarbonates in this study and Figure 4 shows Chondrite-normalized patterns of the samples. Tables 3 and 4 document prominent absorption features for the REE fluorocarbonates and includes probable origins of the features, as chosen through comparison with reflectance spectra from unpublished reagent grade lanthanide oxide spectra, REE-doped calibration standard spectra, and other REE-bearing mineral spectra for which compositional data exists, as well as REE spectroscopy literature. The position and shape of these features were recorded using reflectance spectra (i.e., not continuum removed spectra). Tables 5 and 6 compare significant chemical and spectral differences amongst the bastnaeiste and parisite sample sets, respectively, and include the number of pixels averaged from the sisuROCK imaging scenes by the VNIR and SWIR cameras.

Bastnaesite

Chemical variability amongst the four samples is moderate, with the samples from Burundi (#39382) and Karonga (#56255) showing greater amounts of heavier REE, such as Nd, Sm and Gd (Table 2 and Fig. 4). None of the crystals show unusual concentrations of other cations or notable compositional zoning. Published analyses of bastnaesite from other localities are comparable to the samples analyzed here (e.g., Zaitsev *et al.* 1998, Holtstam and Andersson 2007).

Comparing the spectra (Fig. 5) of the four bastnaesite samples in both the VNIR and SWIR ranges, differences are primarily the relative strengths of absorption features generated by lanthanides. The sample from Sichuan is taken as the baseline because it shows the cleanest spectrum, is derived from the

most number of pixels, and has supporting spectra from a point spectrometer. The sample from Madgascar shows the largest differences in that, in general, its features are more subdued than its peers. Spectra were collected both perpendicular and parallel to the *c*-axis for the Sichuan sample, however, no differences were noted.

Parisite

Chemically, the Snowbird sample shows a greater proportion of heavy rare earth elements (Table 2 and Fig. 4) and especially thorium than the sample from Muzo and neither shows notable compositional zoning. Published analyses of parisite from other localities are comparable to the samples analyzed here (e.g., Zaitsev *et al.* 1998, *Ni et al.* 2000).

Spectra of the two samples show strong similarities (Fig. 6) with variations predominantly in the strength of absorption features and relative depths between specific features. Spectra from Muzo samples also show narrower absorption features. Spectra were collected both perpendicular and parallel to the *c*-axis for both parisite samples, however, no differences were noted.

Synchysite

Three samples of synchysite were studied, however, only the sample from Narsarsuk (Greenland) produced reliable and unambiguous spectra. Spectra indicative of REE-fluorocarbonates could be resolved from the White Cloud Mine (CO, USA) and Morris County (NJ, USA) samples, however, SEM investigations of both revealed complex REE mineralogy, including synchysite, and very fine grained material. Consequently only the Narsarsuk sample is suitable for baseline characterization and

363 discussed in detail. Microprobe results are in accordance with other published analyses (e.g., Forster
364 2001, Guastoni *et al.* 2009).
365
366 The VNIR and SWIR spectra included 1651 pixels and 175 pixels, respectively. The spectrum (Fig. 7)
367 of the Narsarsuk sample is dominated by the high relative concentrations of spectrally active lanthanides
368 and resembles spectra of bastnaesite and parisite. Synchysite shows carbonate related minima at 2337
369 and 2518 nm with a shoulder at 2499 nm.
370

371 DISCUSSION ON THE SPECTRAL VARIABILITY OF REE-FLUOROCARBONATE
372 MINERALS

373 The reflectance spectra from samples of bastnaesite, parisite and synchysite, all members of the REE-
374 fluorocarbonate mineral group, are consistent amongst their respective mineral species. The location of
375 absorption features related to the lanthanides will be a function of the specific REE coordination and
376 asymmetry of crystal structure; because all three minerals have very similar cation sites for the REE
377 consistent patterns were observed. As alluded to in the review of these minerals' crystal structures, the
378 differences in coordination of the CO_3 radical result in the greatest distinction between the REE
379 fluorocarbonates.
380
381 In general, 15 'clusters' of spectral features are present between 500 nm and 2500 nm in bastnaesite, the
382 REE-fluorocarbonate with the highest concentration of REE and simplest crystal structure. Spectra from
383 parisite and synchysite show strong similarities to bastnaesite spectra, however, noise at shorter
384 wavelengths reduces confidence in this region for these two minerals. Tables 3 and 4 document
385 resolvable absorption features of the fluorocarbonates based primarily on spectra from the Sichuan

(bastnaesite), Snowbird (parisite) and Narsarsuk (synchysite) localities. Figures 8 and 9 show representative VNIR and SWIR spectra of bastnaesite, parisite and synchysite with bolded index lines and approximate Full Width at Half Max regions for the dominant absorptions of each group. Probable origins for absorptions are described in Tables 3 and 4.

Intraconfigurational 4f-4f electronic transitions

The REE-related absorptions in the VNIR-SWIR for these LREE-enriched minerals can be largely attributed to Pr^{3+}, Nd^{3+} and Sm^{3+}, with much lesser influence from Eu^{3+}. Trivalent Y, La^{3+} and Lu^{3+} do not have free electrons in the *f* orbitals to generate absorptions, and absorptions related to Ce^{3+} do not fall within the VNIR-SWIR range. Similarly, Gd^{3+} shows absorptions at too high of energy levels, and Dy^{3+}, Tb^{3+}, Ho^{3+}, Er^{3+}, Tm^{3+} and Yb^{3+} are either too low in concentration and/or overlapping with other stronger absorption bands to have a noticeable effect in the spectra of the studied minerals.

Most differences between the REE fluorocarbonate mineral spectra are small shifts in the location of the absorption minima or apparent strengths of overlapping absorptions represented as shoulders or weak local minima. Most of the differences in absorption minima locations are usually on the scale of one or two spectral channels suggesting that in some cases it may be the result of noise or a function of spectrum slope. Noise at shorter wavelengths in spectra from the sisuROCK Imaging Spectrometer precludes delineation of some features below ~650 nm, however, data from the ASD point spectrometer with greater signal to noise performance supports subtle features from 650 nm down to 450 nm. Better resolution of local minima as opposed to overlapping absorptions or shoulders in spectra is primarily observed for bastnaesite over synchysite and parisite, likely because of the greater concentration of REE in the Ca-absent bastnaesite. For example, the local minima at 689 nm and 898 nm (Fig. 8) are generally

409 better defined in the bastnaesite samples, and two resolved absorptions are prevalent with minima at
410 1547 and 1578 nm (Fig. 9). Parisite from Muzo and synchysite from Narsarsuk do, however, show more
411 resolved features than parisite from Snowbird near 676 nm, 889 nm and 1547 nm (Figs. 6 and 7).
412 Bastnaesite consistently shows a deep and relatively broad absorption centered at 1968 nm, while
413 parisite and synchysite both show the minimum of this absorption at 1961 nm. A water combination
414 band occurs in this region and likely plays a role, however, Pr^{3+} also exhibits a strong absorption here.
415 This wavelength shift is consistent with Görller -Walrand and Binnemans (1996) listing this
416 intraconfigurational transition (excitation from ground to the $^7F_2$ multiplet) as being particularly
417 sensitive to the crystal field.
418

419 **Vibrational bands of the carbonate radical**

420 The most important observation amongst the spectra of REE fluorocarbonates is that a distinct
421 absorption at 2243 nm (4458 cm^{-1}) distinguishes bastnaesite from parisite and synchysite, neither of
422 which have this feature (Fig. 8). Bastnaesite also shows a well resolved doublet with absorption bands at
423 2312 and 2324 nm (4325 and 4303 cm^{-1}), a shoulder at 2355 nm (4246 cm^{-1}) and an additional band at
424 2518 nm (3971 cm^{-1}). Notable is that the bastnaesite sample from Madagascar only shows a weak
425 shoulder at 2243 nm and at present the reason for this is uncertain (Fig. 5). It is possible that structurally
426 bound hydroxyl present in the bastnaesite samples may be the origin of the 2243 nm feature, however,
427 the same substitution of fluorine could be said for both parisite and synchysite and neither show this
428 absorption. Furthermore, EMPA composition of the Madagascar sample does not suggest it as being
429 OH-absent and F-rich. Moreover, our unpublished spectra of uncharacterized bastnaesite from other
430 localities do show the 2243 nm absorption feature.
431

Both parisite and synchysite have broader absorption features that are likely related to the carbonate radical. Parisite shows a weak absorption band at 2324 nm (4303 cm^{-1}) and another near 2499 nm (4002 cm^{-1}) (Fig. 9). Synchysite shows a more resolved absorption band at 2337 nm (4279 cm^{-1}) and another at 2518 nm (3971 cm^{-1}).

Spectral effects of the actinides

Most REE minerals will also host the actinide elements Th^{4+} and U^{4+}. The electronic structure of Th^{4+} is similar to La^{3+}, and so has no spectral response related to *f*-orbital transitions. Tetravalent U has a similar structure to Pr^{3+} and Binnemans *et al.* (1999) show that although similar, U^{4+} shows stronger but broader absorption features than Pr^{3+} because the 5*f* electrons are less efficiently shielded in actinides than the 4*f* electrons in lanthanides. Dominant absorptions of U^{4+} have been recorded near ~1111 nm (~9,000 cm^{-1}) and ~666 nm (15,000 cm^{-1}). For the REE fluorocarbonate minerals studied here, Th and U contents were low enough that no actinide-related spectral features were observed. Unpublished spectra of Th-U-bearing zircon do, however, show spectral features in these regions.

IMPLICATIONS

The REE are strategic elements in many high-tech industries due to their special properties in permanent magnets, metal alloys, catalysts and phosphors, among other applications. Recent volatility in supply and demand has increased exploration in North America for these critical elements but ore mineralogy can be significantly variable and can have significant implications for later beneficiation (e.g., Mariano and Mariano 2012).

454 The reflectance spectra of bastnaesite, parisite and synchysite presented and discussed here form the first
455 systematic spectral characterization and comparison of these three important REE minerals. Their
456 spectra are feature-rich, distinct, and comprise many narrow overlapping absorption bands that can be
457 mostly attributed to 4*f*-4*f* intraconfigurational electron transitions of Nd^{3+}, Pr^{3+}, and Sm^{3+} and possibly
458 Eu^{3+}.
459
460 Consistent lanthanide-related spectral responses of the REE fluorocarbonates support the notion that
461 their REE cation site is very similar. Variations in these consistent lanthanide-related responses suggest
462 REE concentration information could be extrapolated from reflectance spectra. Variable carbonate-
463 related spectral responses support the notion that the crystallographic sites for the carbonate radical
464 differ between bastnaesite, synchysite and parisite.
465
466 Exploitable differences for mineral identification using hyperspectral imaging include the carbonate-
467 related absorption at 2243 nm for bastnaesite, as well as a resolved doublet with minima at 2312 nm and
468 2324 nm. Synchysite shows a carbonate-related minimum at 2337 nm and parisite shows a less resolved
469 carbonate-related minimum near 2324 nm. A Pr^{3+} and water related absorption is exhibited at 1968 nm
470 for bastnaesite while in synchysite and parisite it occurs at 1961 nm. Collectively, the spectral patterns
471 of this mineral grouping are distinct from other REE minerals phases, such as monazite, xenotime, and
472 eudialyte, among others.
473
474 This work starts to address the knowledge gap that exists between reflectance spectroscopy and rare
475 earth element mineralogy and future research will include continued characterization and comparison of
476 other important REE-bearing minerals. Accordingly, although hyperspectral remote sensing is becoming

477 increasingly prevalent in the mining and mineral exploration industries, its adoption into REE-focused
478 programs could be of particularly great benefit, such as in defining and assessing ore mineralogy or
479 rapidly logging diamond drill core. Incorporating these spectra into larger spectral databases harnessed
480 by a variety of users will also facilitate the identification of REE fluorocarbonate minerals that may have
481 otherwise gone unnoticed.
482

483 **ACKNOWLEDGEMENTS**

484 We greatly thank A. Mariano and Michel Picard for their supply of samples, knowledge and early
485 discussions. Jilu Feng and Steve Creighton were instrumental with data collection. Financial support is
486 acknowledged from Natural Sciences and Engineering Research Council of Canada. Reviewers Gregg
487 Swayze, Ed Cloutis and Boriana Mihailova provided a thorough and constructive review that greatly
488 improved the quality and clarity of this manuscript.
489

490 **REFERENCES**

491 Adler, H., and Kerr, P.F. (1963) Infrared spectra, symmetry and structure relations of some carbonate
492 minerals. American Mineralogist, 48, 839-853.

493 Bedini, E. (2009) Mapping lithology of the Sarfartoq carbonatite complex, southern West Greenland,
494 using HyMap imaging spectrometer data. Remote Sensing of Environment, 113(6), 1208-1219.

495 Binnemans, K., Couwenberg, I., De Leebeeck, H., Görller-Walrand, C., and Adam, J. L. (1999)
496 Spectroscopic properties of tetravalent uranium in glasses. Journal of Alloys and Compounds,
497 285(1), 105-111.

Bowers, T.L., and Rowan, L.C. (1996) Remote mineralogic and lithologic mapping of the Ice River alkaline complex, British Columbia, Canada, using AVIRIS data. Photogrammetric Engineering and Remote Sensing, 62(12), 1379-1386.

Clark, R.N. (1999) Chapter 1: Spectroscopy of rocks and minerals, and principles of spectroscopy. *In:* Manual of Remote Sensing, Volume 3, Remote Sensing for the Earth Sciences. New York: John Wiley and Sons. 3-58.

Crowley, J., Rowan, L., Podwysocki, M., and Meyer, D. (1988) Evaluation of airborne visible/infrared imaging spectrometer data of the Mountain Pass, California, carbonatite complex. *In*: Proceedings of the Airborne Visible/Infrared Imaging Spectrometer (AVIRIS) performance evaluation workshop. 6-8.

Dieke, G.H., Crosswhite, H.M., and Crosswhite, H. (1968) Spectra and energy levels of rare earth ions in crystals. New York: Interscience Publishers. 401 p.

Förster, H. (2001) Synchysite-(Y)–synchysite-(Ce) solid solutions from Markersbach, Erzgebirge, Germany: REE and Th mobility during high-T alteration of highly fractionated aluminous A-type granites. Mineralogy and Petrology, 72(4), 259-280.

Frost, R.L., and Dickfos, M. J. (2007) Raman spectroscopy of halogen-containing carbonates. Journal of Raman Spectroscopy, 38(11), 1516-1522.

Guastoni, A., Nestola, F., and Giaretta, A. (2009) Mineral chemistry and alteration of rare earth element (REE) carbonates from alkaline pegmatites of Mount Malosa, Malawi. American Mineralogist, 94(8-9), 1216-1222.

Görller-Walrand, C., and Binnemans, K. (1996) Handbook on the Physics and Chemistry of Rare Earths, Elsevier, Amsterdam, Vol. 23, 164 p.

Görller-Walrand, C., and Binnemans, K. (1998) Spectral intensities of f-f transitions, *In:* Handbook on the Physics and Chemistry of Rare Earths, Vol. 25, Chapter 167, editors: K.A. Gschneidner and L. Eyring (North-Holland Publishers, Amsterdam, 1998), 101-264.

Holtstam, D., and Andersson, U.B. (2007) The REE minerals of the Bastnas-type deposits, south-central Sweden. Canadian Mineralogist, 45(5), 1073-1114.

Hunt, G.R. (1977) Spectral signatures of particulate minerals in the visible and near infrared. Geophysics, 42(3), 501-513.

Kerr, A., Rafuse, H., Sparkes, G., Hinchey, J., and Sandeman, H. (2011) Visible/Infrared spectroscopy (VIRS) as a research tool in economic geology: background and pilot studies from Newfoundland and Labrador. Current Research, Newfoundland and Labrador Department of Natural Resources Geological Survey, Report 11-1, 145-166.

Liben, W., Ni, Y., Hughes, J.M., Bayliss, P., and Drexler, J.W. (1994) The atomic arrangement of synchysite-(Ce), $CeCaF(CO_3)_2$. Canadian Mineralogist, 32(4), 865-871.

Liu, G. (2005) Electronic Energy Level Structure. *In:* Spectroscopic Properties of Rare Earths in Optical Materials, Springer Series in Materials Science. 83, 1 – 94.

McHugh, E.L., Girard, J.M., Denes, L.J., Metes, P., and Sabine, C. (2000) Current research on slope movement in mines: use of hyperspectral imagery. *In:* Fourteenth International Conference on Applied Geologic Remote Sensing, Las Vegas, NV, 6-8.

538 Mariano, A.N., and Mariano, A. (2012) Rare earth mining and exploration in North America. Elements,
539 8(5), 369-376.

540 Mars, J.C., and Rowan, L.C. (2011) ASTER spectral analysis and lithologic mapping of the Khanneshin
541 carbonatite volcano, Afghanistan. Geosphere, 7(1), 276-289.

542 Meng., D., Xiuling, W., Tao, M., and Douxing, L. (2001) Determination of six new polytypes in
543 parisite-(Ce) by means of high resolution electron microscopy. Mineralogical Magazine, 65(6),
544 797-797.

545 Miyawaki, R. and Nakai, I. (1996) Crystal chemical aspects of rare earth minerals. *In:* Rare Earth
546 Minerals (A.P. Jones, F. Wall & C.T. Williams, eds). Chapman & Hall, London, U.K., 21-40.

547 Morin Ka, S. (2012) Hyperspectral characterisation of rare earth minerals. Geological Survey of
548 Western Australia, Record 2012/12, 50 p.

549 Ni, Y., Hughes, J.M., and Mariano, A.N. (1993) The atomic arrangement of bastnasite-(Ce), $Ce(CO_3)F$,
550 and structural elements of synchysite-(Ce), rontgenite-(Ce), and parisite-(Ce). American
551 Mineralogist, 78(3-4), 415-418.

552 Ni, Y., Post, J.E., and Hughes, J.M. (2000) The crystal structure of parisite-(Ce),
553 $Ce_2CaF_2(CO_3)_3$. American Mineralogist, 85(1), 251-258.

554 Oppenheimer, C. (1998) Satellite observation of active carbonatite volcanism at Ol Doinyo Lengai,
555 Tanzania. International Journal of Remote Sensing, 19(1), 55-64.

556 Rowan, L.C., Kingston, M.J., and Crowley, J.K. (1986) Spectral reflectance of carbonatites and related
557 alkalic igneous rocks; selected samples from four North American localities. Economic
558 Geology, 81(4), 857-871.

559 Rowan, L.C., Bowers, T.L., Crowley, J.K., Anton-Pacheco, C., Gumiel, P., and Kingston, M.J. (1995)
560 Analysis of airborne visible-infrared imaging spectrometer (AVIRIS) data of the Iron Hill,
561 Colorado, carbonatite-alkalic igneous complex. Economic Geology, 90(7), 1966-1982.

562 Rowan, L.C., and Mars, J.C. (2003) Lithologic mapping in the mountain pass, California area using
563 advanced spaceborne thermal emission and reflection radiometer (ASTER) data. Remote Sensing
564 of Environment, 84(3), 350-366.

565 Yang, H., Dembowski, R.F., Conrad, P.G., and Downs, R.T. (2008) Crystal structure and Raman
566 spectrum of hydroxyl-bastnasite-(Ce), $CeCO_3(OH)$. American Mineralogist, 93(4), 698-701.

567 Zaitsev, A.N, Wall, F., and Bas, M.J.L. (1998) REE-Sr-Ba minerals from the Khibina carbonatites, Kola
568 Peninsula, Russia: their mineralogy, paragenesis and evolution. Mineralogical Magazine, 62(2),
569 225-225.

570

571

572 FIGURE CAPTIONS

573

574 Figure 1. (a) Coordination polyhedron for the Ce1 site in parisite (Ni *et al.* 2000); also applicable to
575 bastnaesite and synchysite. Ce1 (green) atom is coordinated with F1, F2 and F3 (lavender) atoms,
576 whose plane is roughly perpendicular to c-axis, and 6 oxygen (red) atoms O11, O23, O32, O42,
577 O53 and O61. Overall coordination number of 9 in a distorted tricapped trigonal prismatic
578 arrangement. (b) Parisite crystal structure from Ni *et al.* (2000), (c) bastnaesite crystal structure
579 from Ni *et al.* (1993), and (d) synchysite crystal structure from Wang *et al.* (1994). Atom
580 colouring: red=oxygen, green=REE, lavender=F, brown=C. Polyhedra colouring: green=$REEO_6F_3$,
581 dark blue=CaO_8, brown=CO_3.

582

583 Figure 2. Bond characteristics for the CO_3 radical polyhedra in REE fluorocarbonate. Data from Table 1
584 and references therein, Min=minimum, Mid=middle, Max=maximum.

585

586 Figure 3. (a) Hyperspectral imagery of the synchysite-bearing sample from Narsarsuk in the short wave
587 infrared (SWIR). (b) Mixture tuned matched filtering (MTMF) results for synchysite in SWIR
588 scene and (c) regions of interest (ROI) derived from thresholded MTMF results for generating an
589 average spectrum. (d) Annotated digital photograph of the same sample from nominally the same
590 perspective. Arrows in (c) and (d) point to the same patches of synchysite. Monomineralic patches
591 of synchysite are on the order of 2 mm by 2 mm, large enough for successful imaging with a
592 spatial resolution of 0.241 mm by 0.241 mm, to enable isolation of pure monomineralic pixels
593 with confidence for averaging of their spectra.

Figure 4. Chondrite-normalized REE plot from microprobe results. Normalization values from McDonough and Sun (1995). Erbium (Er), Tm, Yb and Lu are below detection for all samples.

Figure 5. Stacked spectra of bastnaesite in VNIR (left, 500 to 1000 nm) and SWIR (right, 975 to 2530 nm) from the two sisuROCK instrument cameras. Spectra from top to bottom: Sichuan (S), Burundi (B), Madagascar (M), Karonga (K).

Figure 6. Stacked spectra of parisite in VNIR (left, 500 to 1000 nm) and SWIR (right, 975 to 2530 nm) from the two sisuROCK instrument cameras. Spectra from top to bottom: Muzo (M), Snowbird (SB).

Figure 7. Spectra of synchysite from Narsarsuk in VNIR (left, 500 to 1000 nm) and SWIR (right, 975 to 2530 nm) from the two sisuROCK instrument cameras.

Figure 8. VNIR (500 to 1000 nm) spectra of bastnaesite (B, top), parisite (P, middle) and synchysite (S, bottom). Italic numbers denote groups with probable origin described in Table 3. Lines denote prominent absorption features with wavelength position, shaded boxes represent the approximate Full Width at Half Max for each absorption or absorption cluster, borderless box indicates narrow feature. Stacked spectra from sisuROCK instrument.

Figure 9. SWIR (975 to 2530 nm) spectra of bastnaesite (B, top), parisite (P, middle) and synchysite (S, bottom). Italic numbers denote groups with probable origin described in Table 4. Lines denote

617 prominent absorption features with wavelength position, shaded boxes represent the approximate
618 Full Width at Half Max for each absorption or absorption cluster, borderless box indicates narrow
619 feature. Stacked spectra from sisuROCK instrument.
620

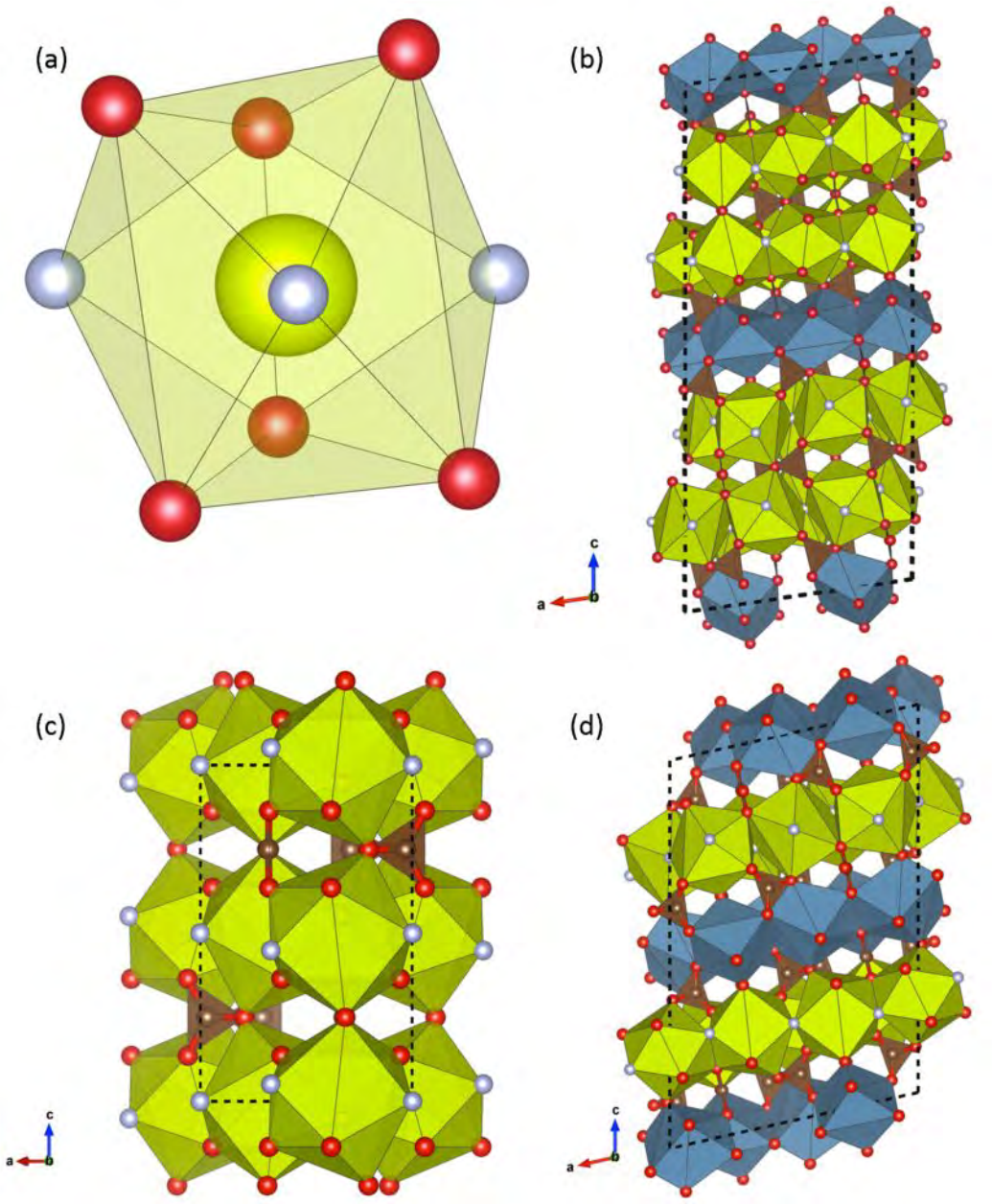
(a)
(b)
c
a
(c)
c
a
(d)
c
a

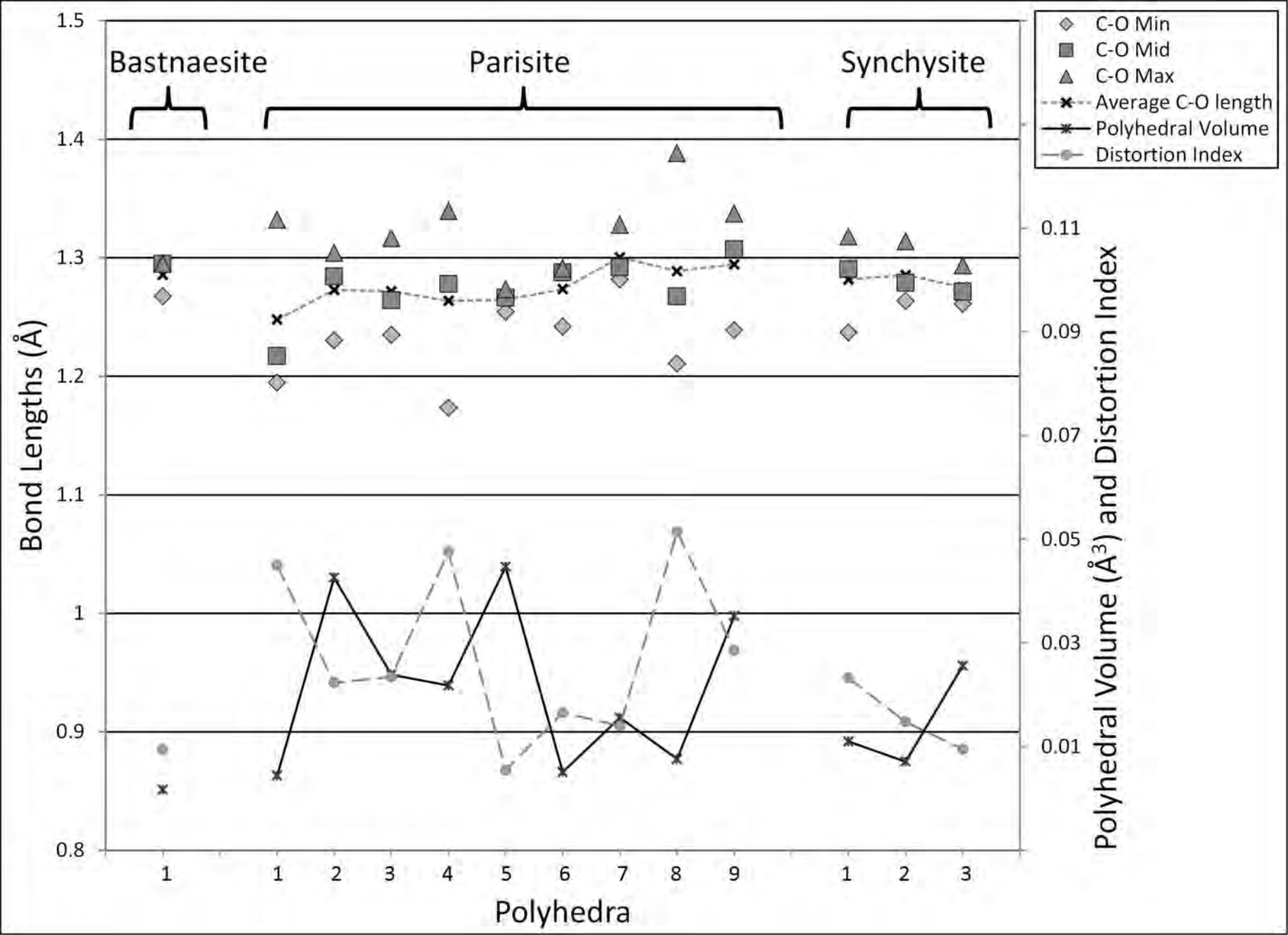
Bastnaesite
Parisite
Synchysite
C-O Min
C-O Mid
C-O Max
Average C-O length
Polyhedral Volume
Distortion Index
Bond Lengths (Å)
Polyhedral Volume (Å3) and Distortion Index
Polyhedra
1.5
1.4
1.3
1.2
1.1
1
0.9
0.8
0.11
0.09
0.07
0.05
0.03
0.01
1
1
2
3
4
5
6
7
8
9
1
2
3

(a) SWIR False Colour

(b) MTMF Value Colour Ramp

(c) SWIR with ROI from MTMF

(d) Digital Photo

1 cm

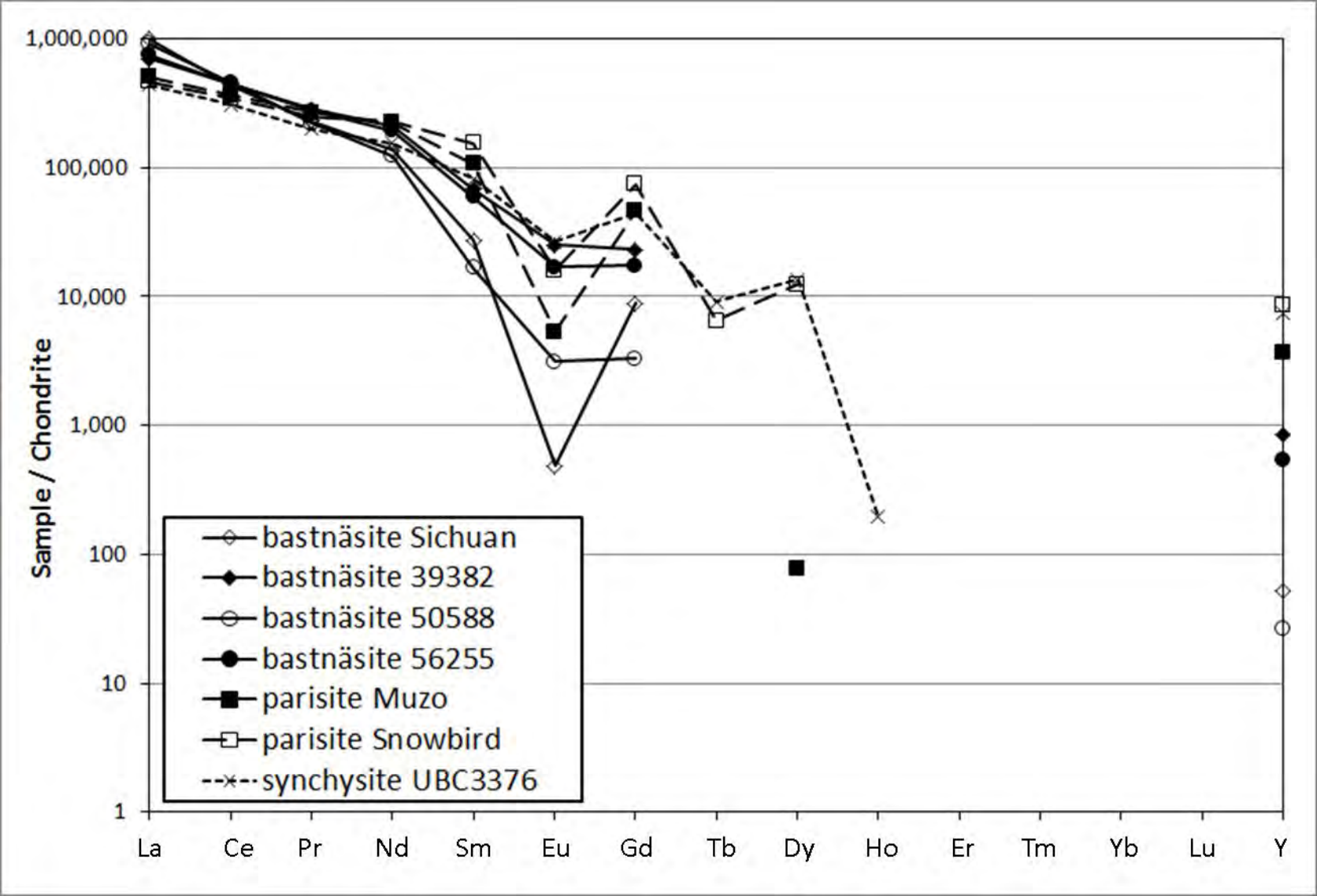
1,000,000
100,000
10,000
1,000
100
10
1
Sample / Chondrite
La
Ce
Pr
Nd
Sm
Eu
Gd
Tb
Dy
Ho
Er
Tm
Yb
Lu
Y
bastnäsite Sichuan
bastnäsite 39382
bastnäsite 50588
bastnäsite 56255
parisite Muzo
parisite Snowbird
synchysite UBC3376

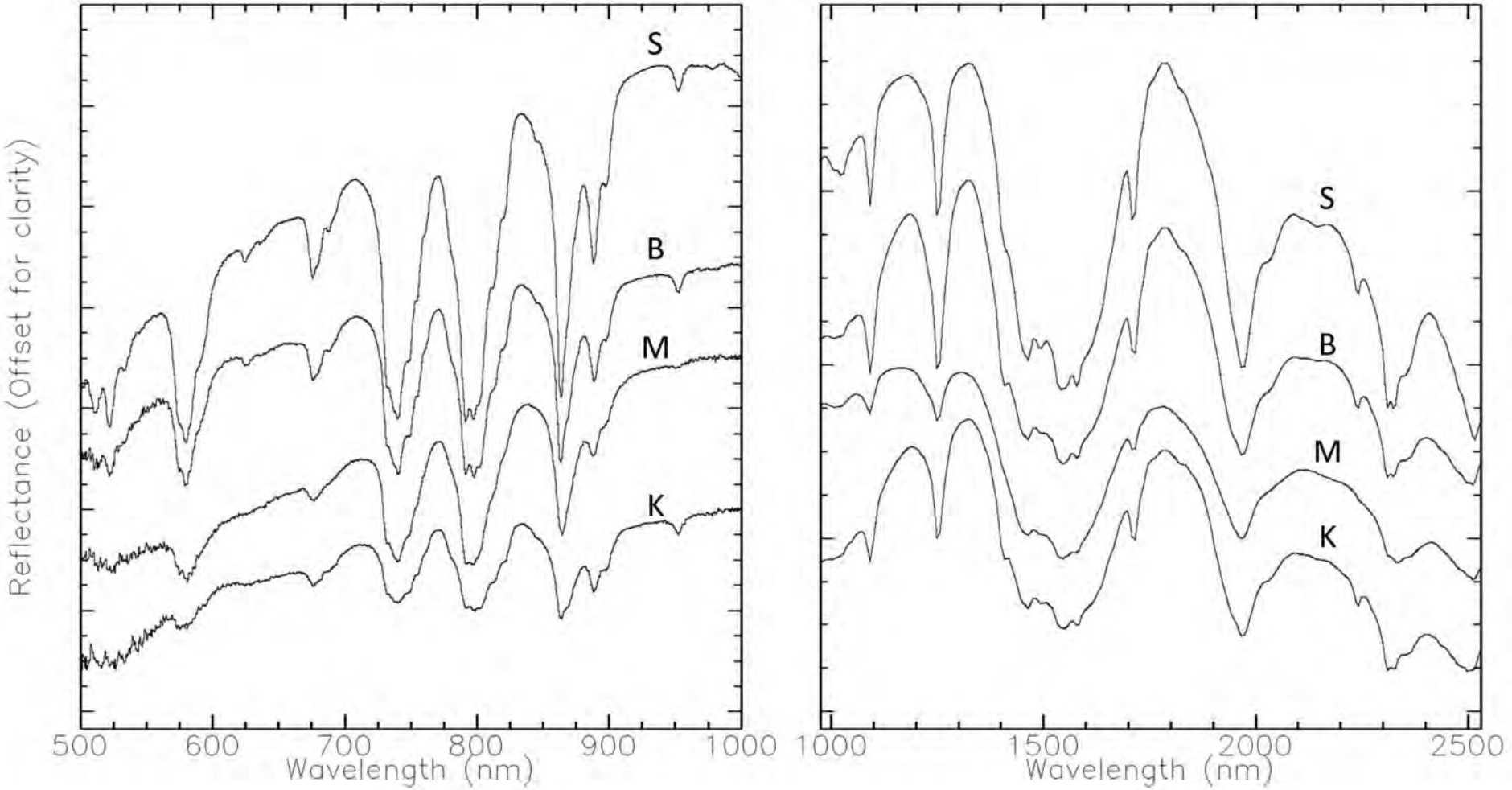
Reflectance (Offset for clarity)
S
B
M
K
500
600
700
800
900
1000
Wavelength (nm)
S
B
M
K
1000
1500
2000
2500
Wavelength (nm)

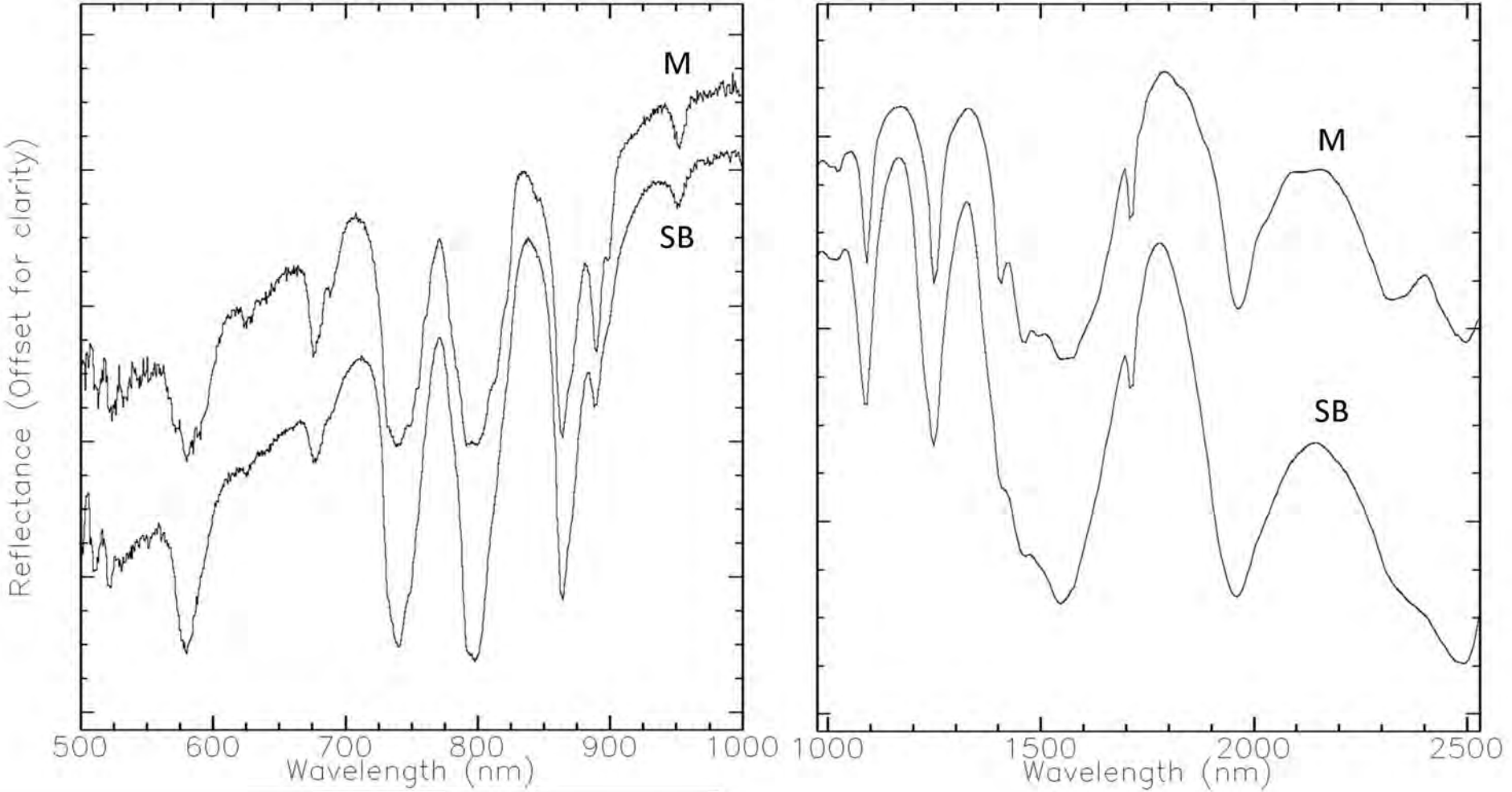
M
SB
Reflectance (Offset for clarity)
500
600
700
800
900
1000
Wavelength (nm)
M
SB
1000
1500
2000
2500
Wavelength (nm)

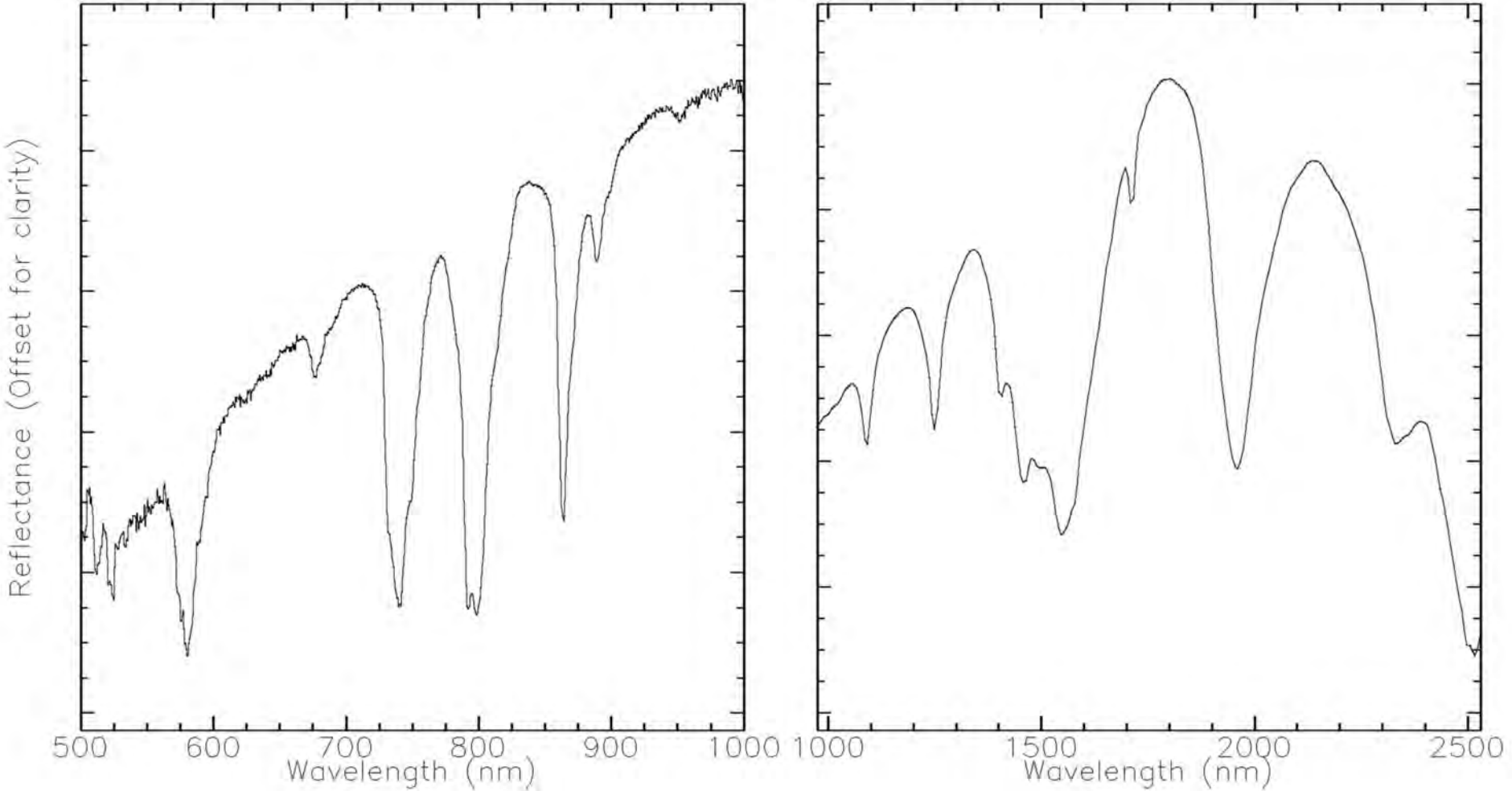
Reflectance (Offset for clarity)
500
600
700
800
900
1000
Wavelength (nm)
1000
1500
2000
2500
Wavelength (nm)

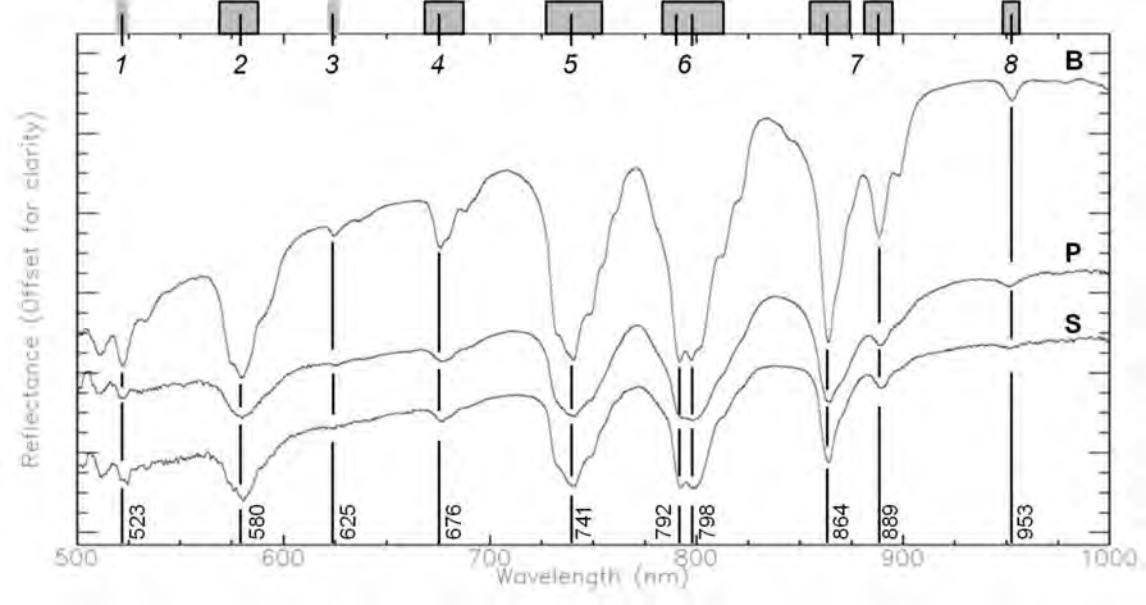
1
2
3
4
5
6
7
8
B
P
S
523
580
625
676
741
792
798
864
889
953
500
600
700
800
900
1000
Wavelength (nm)
Reflectance (Offset for clarity)

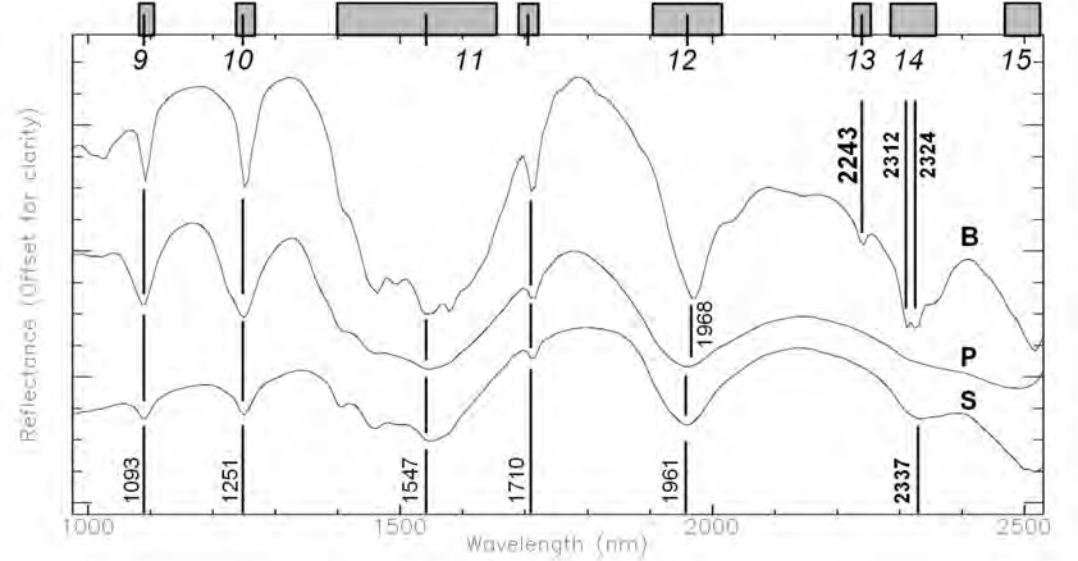
9
10
11
12
13
14
15
2243
2312
2324
B
P
S
1968
1093
1251
1547
1710
1961
2337
Reflectance (Offset for clarity)
1000
1500
2000
2500
Wavelength (nm)

Table 1. Some basic properties of the REE fluorocarbonates

Mineral	bastnaesite	parisite	synchysite
Reference	Ni *et al.* (1993)	Ni *et al.* (2000)	Wang *et al.* (1994)
Formula	$REECO_3F$	$CaREE_2(CO_3)_3F_2$	$CaREE(CO_3)_2F$
Symmetry	Hexagonal	Monoclinic	Monoclinic
Space group	$P\bar{6}2c$	Cc	C2/c
a (Å)	7.1175	12.305	12.329
b (Å)		7.1053	7.110
c (Å)	9.7619	28.25	18.741
B (°)		98.257	102.68
Structure			
REE coordination	9: 3*F, 6*O	9: 3*F, 6*O	9: 3*F, 6*O
REE site shape	tricapped trigonal	tricapped trigonal	tricapped trigonal
Number of unique REE cation sites	1	6	2
REE-O (Min, Å)	2.542	2.466	2.497
REE-O (Mean, Å)	2.571	2.564	2.558
REE-O (Max, Å)	2.591	2.631	2.619
REE-F (Min, Å)	2.403	2.370	2.376
REE-F (Mean, Å)	2.407	2.397	2.399
REE-F (Max, Å)	2.416	2.445	2.417
CO_3 influences	Each CO_3 layer influenced by REE only	3 distinct CO_3 layers, one influenced by REE only, two influenced by REE and Ca	Each CO_3 layer influenced by Ca and REE
Number of unique CO_3 polyhedra	1	9	3
Average C-O bond lengths (Å)			
CO_3 #1	1.287	1.2478	1.2817
CO_3 #2		1.2728	1.2854
CO_3 #3		1.2718	1.2752
CO_3 #4		1.2636 [a]	
CO_3 #5		1.2646 [a]	
CO_3 #6		1.2736 [a]	
CO_3 #7		1.3004	
CO_3 #8		1.2887	
CO_3 #9		1.2945	
Average CO_3 polyhedra volume ($Å^3$)	0.0017	0.0223	0.0146
Average CO_3 polyhedra distortion index	0.0094	0.0282	0.0159
General chemistry			
REE_2O_3 wt%	73	59	51
CaO wt%	0	10.5	17
F wt%	5	4.5	2.6
CO_3 wt%	20	24	28

[a] These CO_3 polyhedra in parisite are coordinated only to REE

Table 2. Average EMPA compositions of REE fluorocarbonate samples in wt%

Mineral	bastnäsite		bastnäsite		bastnäsite		bastnäsite		parisite		parisite		synchysite		
Sample ID	Sichuan		39382		50588		56255		Muzo		Snowbird		UBC3376		
Locality	Diao Lou Shan, China		Burundi		Madagascar		Karonga, Congo		Colombia		Montana, USA		Narsarsuk, Greenland		Detection Limits
n	*10*	2σ	*5*	2σ	*5*	2σ	*5*	2σ	*6*	2σ	*5*	2σ	*3*	2σ	(average)
Nb_2O_5	0.01	0.02	0.00	0.00	0.01	0.03	0.00	0.00	0.00	0.02	0.00	0.01	0.00	0.00	0.04
P_2O_5	0.00	0.00	0.00	0.00	0.00	0.00	0.00	0.02	0.00	0.00	0.00	0.00	0.05	0.17	0.02
SiO_2	0.05	0.01	0.11	0.02	0.06	0.00	0.11	0.01	0.06	0.01	0.08	0.08	0.38	0.52	0.01
ZrO_2	0.00	0.00	0.01	0.03	0.00	0.00	0.01	0.03	0.00	0.00	0.00	0.00	0.01	0.03	0.04
UO_2	0.53	0.10	0.00	0.00	0.00	0.00	0.00	0.00	0.39	0.13	0.34	0.19	0.00	0.00	0.07
ThO_2	0.14	0.13	0.00	0.00	0.37	0.48	0.00	0.00	0.83	0.64	1.62	0.26	0.54	0.12	0.06
Al_2O_3	0.00	0.00	0.00	0.00	0.00	0.00	0.00	0.00	0.00	0.00	0.00	0.00	0.04	0.15	0.01
La_2O_3	27.77	1.88	19.44	1.00	25.22	0.64	20.76	0.75	14.03	0.53	12.87	0.37	12.17	1.33	0.03
Ce_2O_3	31.14	0.67	32.58	0.31	32.95	0.11	32.47	0.48	26.11	0.90	24.77	0.77	22.29	0.99	0.02
Pr_2O_3	2.50	0.32	3.07	0.33	2.38	0.19	2.98	0.15	2.90	0.19	2.71	0.19	2.17	0.29	0.02
Nd_2O_3	7.25	1.18	11.05	1.07	6.62	0.15	10.28	0.20	11.90	0.59	12.14	0.17	8.25	0.57	0.02
Sm_2O_3	0.47	0.18	1.18	0.14	0.29	0.07	1.02	0.01	1.85	0.14	2.64	0.23	1.42	0.05	0.02
Eu_2O_3	0.00	0.02	0.16	0.08	0.02	0.05	0.11	0.05	0.03	0.07	0.10	0.10	0.17	0.01	0.02
Gd_2O_3	0.20	0.18	0.53	0.14	0.08	0.10	0.40	0.10	1.06	0.19	1.70	0.25	1.03	0.08	0.02
Tb_2O_3	0.00	0.00	0.00	0.00	0.00	0.00	0.00	0.00	0.00	0.00	0.03	0.08	0.04	0.02	0.02
Dy_2O_3	0.00	0.00	0.00	0.00	0.00	0.00	0.00	0.00	0.00	0.01	0.35	0.16	0.38	0.08	0.02
Ho_2O_3	0.00	0.00	0.00	0.00	0.00	0.00	0.00	0.00	0.00	0.00	0.00	0.00	0.001	0.00	0.02
Er_2O_3	0.00	0.00	0.00	0.00	0.00	0.00	0.00	0.00	0.00	0.00	0.00	0.00	0.00	0.00	0.02
Tm_2O_3	0.00	0.00	0.00	0.00	0.00	0.00	0.00	0.00	0.00	0.00	0.00	0.00	0.00	0.00	0.02
Yb_2O_3	0.00	0.00	0.00	0.00	0.00	0.00	0.00	0.00	0.00	0.00	0.00	0.00	0.00	0.00	0.03
Lu_2O_3	0.00	0.00	0.00	0.00	0.00	0.00	0.00	0.00	0.00	0.00	0.00	0.00	0.00	0.00	0.02
Y_2O_3	0.01	0.03	0.17	0.12	0.01	0.01	0.11	0.06	0.74	0.32	1.69	0.13	1.47	0.53	0.04
SrO	0.01	0.04	0.02	0.06	0.08	0.13	0.02	0.05	0.00	0.00	0.00	0.00	0.22	0.36	0.03
MgO	0.00	0.00	0.02	0.02	0.01	0.02	0.01	0.02	0.00	0.00	0.00	0.00	0.00	0.00	0.01
FeO	0.00	0.00	0.00	0.00	0.00	0.00	0.00	0.00	0.00	0.00	0.00	0.00	0.17	0.43	0.01
CaO	0.11	0.10	0.00	0.00	0.05	0.02	0.00	0.00	10.48	1.06	10.23	0.16	16.49	2.69	0.01
Na_2O	0.03	0.03	0.00	0.00	0.00	0.00	0.00	0.00	0.01	0.02	0.01	0.01	0.10	0.04	0.01
Cl	0.01	0.02	0.08	0.02	0.06	0.02	0.08	0.04	0.02	0.01	0.02	0.01	0.12	0.05	0.01
F	5.22	0.42	4.42	0.22	4.56	0.15	4.27	0.23	4.48	0.20	4.12	0.57	2.87	1.04	0.02
CO_2*	18.86		18.36		18.32		18.35		24.2		24.46		27.26		

H_2O**	1.38	1.64	1.57	1.17	1.17	1.38	1.4
-O≡Cl	0.00	-0.02	-0.01	-0.02	0.00	0.00	-0.03
-O≡F	-2.20	-1.86	-1.92	-1.80	-1.89	-1.73	-1.21
Total	93.50	90.96	90.73	90.32	98.37	99.51	97.80
$[REE+Y]_2O_3$	*69.35*	*68.19*	*67.57*	*68.12*	*58.61*	*58.99*	*49.38*

Ta, Ti, Mn, K and Ba were sought but not detected
*Determined by stoichiometry, on the basis of 4, 11 and 7 anions, respectively
**H2O calculated assuming ideal occupation of "F" site (F, Cl, OH)

Table 3. Prominent absorption features of the REE fluorocarbonates in the VNIR range.

	Bastnaesite		**Parisite**		**Synchysite**		**Probable Origin**
Group	λ (nm)	Shape	λ (nm)	Shape	λ (nm)	Shape	
	500	MIN	501	MIN-n	503	MIN-n	Nd^{3+}
1	511	MIN	510	MIN-n	512	MIN-n	Nd^{3+}
	523	**MIN**	**523**	**MIN**	**525**	**MIN-n**	**Nd^{3+}**
	533	MIN-w	533	MIN-n	534	MIN-n	Nd^{3+}>Eu^{3+}
	545	SH	545	SH-n			Nd^{3+}
	557	MIN-w					Sm^{3+}
2	575	SH	574	SH-n	576	SH-n	Nd^{3+}
	580	**MIN-st**	**580**	**MIN-st**	**580**	**MIN-st**	**Nd^{3+}**
	595	SH	595	SH	595	SH	Nd^{3+}>Pr^{3+}
3	**625**	**MIN**	**625**	**MIN-w**	**625**	**MIN-w, n**	**Nd^{3+}**
	636	MIN-w	637	MIN-w, n			Nd^{3+}
	642	SH-w					Nd^{3+}
4	**676**	**MIN**	**676**	**MIN**	**678**	**MIN**	**Nd^{3+}**
	681	SH	681	MIN-w, n	680	SH	Nd^{3+}
	689	MIN-w	689	MIN-w	691	SH	Nd^{3+}
	693	SH					Nd^{3+}
5	734	SH	732	SH	732	SH	Nd^{3+}
	738	SH	738	SH	738	SH	Nd^{3+}
	741	**MIN-st**	**741**	**MIN-st**	**740**	**MIN-st**	**Nd^{3+}**
	749	MIN-w	749	SH	749	SH	Nd^{3+}
	755	SH	755	SH	756	SH	Nd^{3+}
	761	SH	762	SH	762	SH	Nd^{3+}
	768	SH	770	SH	770	SH	Nd^{3+}
6	781	SH	781	SH	780	SH	Nd^{3+}
	784	SH-w	784	SH-w	784	SH-w	Nd^{3+}
	792	**MIN-db**	**792**	**MIN-db**	**792**	**MIN-db**	**Nd^{3+}**
	797	**MIN-db**	**798**	**MIN-db**	**799**	**MIN-db**	**Nd^{3+}**
	803	SH	804	SH	804	SH	Nd^{3+}
	813	SH	813	SH	813	SH	Nd^{3+}
	821	SH	822	SH	822	SH	Nd^{3+}
7	845	SH	845	SH			Nd^{3+}
	864	**MIN-st**	**864**	**MIN-st**	**864**	**MIN-st**	**Nd^{3+}**
	871	SH	871	SH	871	SH	Nd^{3+}
	889	**MIN**	**889**	**MIN**	**889**	**MIN**	**Nd^{3+}**
	898	MIN-w	899	SH	899	SH	Nd^{3+}
8	**953**	**MIN**	**953**	**MIN**	**953**	**MIN-w**	**Sm^{3+}**
	978	MIN-w	978	SH-w			Nd^{3+}>Pr^{3+}

Bolded values are indexed on Fig 8. Shape and modifier abbreviations: MIN=local minimum, SH=shoulder, -n=noisy, -w=weak, -st=strong, -db=doublet.

Table 4. Prominent absorption features of the REE fluorocarbonates in the SWIR range.

	Bastnaesite		**Parisite**		**Synchysite**		**Probable Origin**
Group	λ (nm)	Shape	λ (nm)	Shape	λ (nm)	Shape	
9	1004	MIN-w	1004	SH-w	998	SH-w	Pr^{3+}
	1023	MIN	1023	MIN-w	1023	SH	Pr^{3+}
	1093	**MIN-st**	**1093**	**MIN-st**	**1093**	**MIN-st**	**Sm^{3+}**
10	1225	SH-w	1225	SH-w	1225	SH-w	Sm^{3+}
	1251	**MIN-st**	**1251**	**MIN-st**	**1251**	**MIN-st**	**Sm^{3+}**
	1314	SH-w	1314	SH-w	1301	SH-w	Pr^{3+}?
11	1408	SH	1408	MIN-w	1408	MIN-w	H_2O
	1465	MIN	1465	MIN	1459	MIN	Pr^{3+}
	1496	MIN-w	1496	MIN-w	1496	MIN-w	**Pr^{3+}>Sm^{3+}**
	1547	**MIN-st**	**1547**	**MIN**	**1547**	**MIN-st**	**Pr^{3+}>Sm^{3+}**
	1578	**MIN**	1578	**SH**	1578	**SH**	**Pr^{3+}>Sm^{3+}>Nd^{3+}**
	1666	SH-w	1666	SH-w	1666	SH-w	Nd^{3+}
	1710	**MIN**	**1710**	**MIN**	**1710**	**MIN**	**Nd^{3+}**
	1742	SH-w	1742	SH-w	1742	SH-w	Nd^{3+}
	1761	SH-w	1767	SH-w	1767	SH-w	Nd^{3+}
	1817	SH-w	1817	SH-w	1817	SH-w	Nd^{3+}
	1886	SH-w	1880	SH-w			Pr^{3+}?
	1943	SH-w					Pr^{3+}
12	**1968**	**MIN-st**	**1961**	**MIN-st**	**1961**	**MIN-st**	**Pr^{3+}>Sm^{3+} & H_2O**
	2037	SH	2037	SH-w	2037	SH-w	Pr^{3+}>Eu^{3+}
	2112	SH-w	2118	SH-w	2105	SH-w	CO3?
	2143	MIN-w	2143	SH-w			Pr^{3+}
13	2243	**MIN-st**		**ABSENT**		**ABSENT**	**CO_3**
14	**2312**	**MIN-db**	2312	SH	2312	SH-w	CO_3>Pr^{3+}>Nd^{3+}>Sm^{3+}
	2324	**MIN-db**	**2324**	**MIN / SH**	**2337**	**MIN**	**CO_3>Pr^{3+}>Nd^{3+}>Sm^{3+}**
	2355	SH	2355	SH-w	2368	SH-w	CO_3>Pr^{3+}>Nd^{3+}>Sm^{3+}
			2393	SH-w	2393	MIN-w	CO_3
15	2437	SH	2443	SH-w			CO_3>Pr^{3+}>Nd^{3+}>Sm^{3+}
	2480	SH-w	2474	SH	2474	SH-w	CO_3
	2499	SH-w	2499	MIN	2499	SH	CO_3
	2518	MIN	2518	SH-w	2518	MIN	CO_3

Bolded values are indexed on Fig 9. Shape and modifier abbreviations: MIN=local minimum, SH=shoulder, -n=noisy, -w=weak, -st=strong, -db=doublet.

Table 5. Significant chemical and spectral differences between bastnaesite samples.

Sample	VNIR pixels	SWIR pixels	Notes
Diao Loa Shan – Sichuan, China	5715	4379	Chemically, shows intermediate values for REE. Spectrally, shows the most resolved features in the VNIR.
Burundi	2312	173	Chemically, shows the highest values for heavier REE, such as Gd. Spectrally, is very similar to the Sichuan sample. The 1093 nm and 1251 nm absorptions (Sm^{3+} related) are particularly pronounced in the suite, which is correlative with this sample having the highest Sm content. Accordingly, the Sm^{3+} related 1408 nm feature is represented as a local minimum rather than a shoulder
Madagascar	613	387	Chemically, shows higher La and Ce but lower middle REE within the bastnaesite suite. Spectrally, it generally shows subdued REE absorptions as compared to other samples. However, a significant difference is that the carbonate related 2243 nm and 2312/2324 nm doublet features are very subdued.
Karonga Mine, Congo	1341	135	Chemically, shows intermediate values for REE with a greater abundance of middle REE than the Sichuan sample. Spectrally, it is similar to the Burundi sample with respect to the 1093, 1251 and 1408 nm Sm^{3+} features, however, it displays less resolved Nd^{3+} related features at 741, 792/797 and 864 nm.

Table 6. Significant chemical and spectral differences between parisite samples.

Sample	VNIR pixels	SWIR pixels	Notes
Muzo, Colombia	265	162	Chemically, more enriched in La, Ce and Pr. Spectrally, tends to show better resolved and narrower features than for the Snowbird sample.
Snowbird, USA	2130	1790	Chemically, shows greater values for heavier REE, from Nd to Lu, but is still LREE-enriched. Spectrally, it shows broadened features and finer structure is generally subdued (e.g., clusters near 580 nm and 1500 nm). The carbonate-realted features near 2324 and 2474 nm are also less resolved. The sample's greater amount of Th will have subjected these crystals to greater radioactivity, which might contribute to broadening of spectral features as the crystal loses crystallinity.